



Original paper

Segmentation improvement through denoising of PET images with 3D-context modelling in wavelet domain

Carlos Huerga^{a,*}, Luis Glaría^b, Pablo Castro^c, Luis Alejo^a, José Bayón^a, Eduardo Guibelalde^d

^a Medical Physics and Radiation Protection Service, Hospital Universitario La Paz, Paseo de la Castellana 261, 28046 Madrid, Spain

^b Radiation Oncology Service, Hospital Universitario La Paz, Paseo de la Castellana 261, 28046 Madrid, Spain

^c Medical Physics Department, Hospital Universitario de La Princesa, C/Diego de León 62, 28006 Madrid, Spain

^d Department of Radiology, Faculty of Medicine, Complutense University, Avenida Complutense, s/n, 28040 Madrid, Spain

ARTICLE INFO

Keywords:

Positron emission tomography
3D wavelet transform
Denoising
Segmentation

ABSTRACT

Positron emission tomography (PET) images have been incorporated into the radiotherapy process as a powerful tool to assist in the contouring of lesions, leading to the emergence of a broad spectrum of automatic segmentation schemes for PET images (PET-AS). However, not all proposed PET-AS algorithms take into consideration the previous steps of image preparation. PET image noise has been shown to be one of the most relevant affecting factors in segmentation tasks. This study demonstrates a nonlinear filtering method based on spatially adaptive wavelet shrinkage using three-dimensional context modelling that considers the correlation of each voxel with its neighbours. Using this noise reduction method, excellent edge conservation properties are obtained. To evaluate the influence in the segmentation schemes of this filter, it was compared with a set of Gaussian filters (the most conventional) and with two previously optimised edge-preserving filters. Five segmentation schemes were used (most commonly implemented in commercial software): fixed thresholding, adaptive thresholding, watershed, adaptive region growing and affinity propagation clustering. Segmentation results were evaluated using the Dice similarity coefficient and classification error. A simple metric was also included to improve the characterisation of the filters used for induced blurring evaluation, based on the measurement of the average edge width. The proposed noise reduction procedure improves the results of segmentation throughout the performed settings and was shown to be more stable in low-contrast and high-noise conditions. Thus, the capacity of the segmentation method is reinforced by the denoising plan used.

1. Introduction

Radiotherapeutic process is highly dependent on digital image in many stages of its process. From the prescription to the follow-up of the treatment [1].

Thus, new procedures appear to help in the interpretation and analysis. In general, image segmentation performs an important function in medical image processing and analysis [2]. In radiotherapy, these tasks have an essential role.

The positron emission tomography (PET) image has become a powerful tool, providing functional information on radiotracer localisation and extension in pathological regions [3], making it fundamental in the radiotherapeutic process, which needs to precisely contour regions of pathological uptakes for helping to define target volumes. The PET image is characterised by a low signal-to-noise ratio (SNR) and blurred edges in comparison with other modalities (CT or MRI). Small

volumes are affected by the partial volume effect (PVE) [4], a limiting characteristic of PET images; thus, image preparation is necessary prior to segmentation. In many cases, this stage includes the application of noise reduction procedures.

Noise is one of the most relevant affecting factors in segmentation [5], and the noise reduction method is one of the keys to its application. The effectiveness of maintaining the uptake magnitude is one of the challenges facing denoising algorithms for PET images. The algorithm used must also preserve the edges to prevent contour modification of the objects and as well as prevent changes in the volumes of interest.

However, the recent Report of American Association of Physicists in Medicine (AAPM) Task Group No. 211 [6] shows that few authors provide information on presegmentation processing. The study by Geets et al. [7] is one of the few that explicitly includes this stage of pre-processing in the segmentation framework. In this study, the denoising process is performed within the segmentation framework, as a previous

* Corresponding author.

E-mail address: carlos.huerga@salud.madrid.org (C. Huerga).

<https://doi.org/10.1016/j.ejmp.2018.08.008>

Received 23 March 2018; Received in revised form 22 May 2018; Accepted 12 August 2018

Available online 16 August 2018

1120-1797/ © 2018 Associazione Italiana di Fisica Medica. Published by Elsevier Ltd. All rights reserved.

step, by applying a bilateral filter (bf) and using a deblurring process to compensate for the effect of the system's point spread function (psf). Other authors [8,9] have used anisotropic diffusion filtering (adf) during the preparation stage of the image. The use of adf prevents blurring of the object's edges and preserves the average activity within a region. A combined approach of noise reduction and the process of segmentation by means of wavelets is shown in a study by Hanzouli et al. [10], using the anatomical information of the CT. The sensitivity of the segmentation process with the choice of the postreconstruction filter has been demonstrated by McGurk et al. [11], showing that the choice of the filter can produce wide variations in segmentation accuracy depending on the method used. Taking into account the previous Report of the AAPM [6], relatively few authors focus on the filtering process as a necessary step prior to segmentation; those who do, however, agree to use filtering procedures with favourable edge preservation properties.

We have proposed a wavelet-based noise reduction technique [12] with the ability to maintain uptake values while preserving the edges in "significant" regions (determining the local variance through the correlation of pixels and adapting the denoising process to the context). In this study, the extension to 3D was estimated by averaging the various directions of each voxel. We are proposing in the following paper an improvement when obtaining the relation of each voxel with its context directly in 3D (full 3D). This algorithm has two important features that make it especially interesting in segmentation tasks.

The first feature is significant noise reduction in the background regions, which had been outlined in the previous study, with an increase in contrast between various tissues (liver, lung, mediastinum) being considered as reference [13]. The second essential feature is edge preservation, which is crucial in segmentation tasks. This property is improved when the relationship of each voxel with its 3D surroundings is evaluated.

In this study, the capabilities of the improved noise reduction algorithm under various automatic PET segmentation schemes (PET-AS) are shown. In order to accomplish this demonstration, the denoising method we proposed has been compared with other methods of noise reduction frequently used in this process, showing how the efficacy of the segmentation method is reinforced by the used denoising plan.

2. Materials and methods

2.1. Datasets and ground truth

Various image datasets were used to show the effect of filtering using various methods of segmentation in a wide variety of images with various resolutions and various signal-to-background (S/B) ratios and noise levels. International Electrotechnical Commission (IEC) phantom images with hot inserts were used, considering various S/B ratios. The evaluation mask (the "Ground Truth") was determined by manual segmentation in CT images using a spherical 3D region of interest (ROI) which was later downsampled. This phantom was not without some limitations [6]; among others, the wall effect on the inserts [14] and its regular shape. Taking into account both considerations, a synthetic phantom with highly irregular lesions and a high number of radioactive environments was used. The evaluation mask in this case was the contour used for the generation of the lesion. In order to introduce an approximation to the clinical situation, simulated lesions were generated in six patients and were postprocessed with each filter. To assess the influence of filtering on manual contouring, lesions of known size dimensions were contoured by an expert radiotherapy oncologist. The details of each data set are reported below.

2.1.1. IEC phantom series: spherical objects

A NEMA IEC Body methacrylate Phantom 2001 was used, simulating a human thorax. It has an internal length of 194 mm and contains six spheres with internal diameters of 10, 13, 17, 22, 28 and 37 mm and

a wall thickness of 1 mm. It includes a cylindrical cold central insert 180 mm in length and 51 mm in diameter. To simulate lesions of various sizes in distinct radioactive environments, the thorax volume was filled with variable activity concentrations of 18F, from 7.1 kBq ml⁻¹ to 23.3 kBq ml⁻¹; and the spheres were subsequently filled with an approximate concentration of 115 kBq ml⁻¹. Three scenarios were considered with approximate (S/B) ratios of 20:1 (high contrast), 10:1 (medium contrast) and 5:1 (low contrast).

The acquisitions were performed using a GE Discovery LS PET/CT scanner (General Electric Medical Systems, Milwaukee, USA). This hybrid scanner combines CT multislice LightSpeed with an 18-ring (14.5 cm) PET Advance NXi with bismuth germanate detector blocks. The PET data were acquired in two-dimensional mode, with a field of view of 50 cm and 4 min scan time. The PET images were reconstructed with CT-based attenuation correction without PSF correction, using the iterative ordered subset expectation maximisation (OSEM) method, with two iterations and 28 subsets. The PET images were reconstructed in a 128 × 128 matrix (35 slices) with a voxel size of 3.906 mm × 3.906 mm × 4.250 mm.

With this pixel size, some algorithms were unable to segment the smaller spheres. This becomes noticeable in low-contrast scenarios. Therefore, an extra reconstruction was performed in a 256 × 256 matrix with a voxel size of 1.953 mm × 1.953 mm × 4.250 mm for the low-contrast case. This acquisition was named ~5:1 HR (low contrast and high resolution).

2.1.2. Simulated phantom series: irregular objects

Synthetic images were built using the PETSTEP simulator [15]. PETSTEP is a series of open-source routines developed in the Matlab environment (MathWorks, Natick, MA). PETSTEP operates in the framework of the computational environment for radiotherapy research (CERR) [16]. A GE Discovery 690 PET/CT scanner was modelled, using images of a 20-cm diameter cylindrical phantom, where irregular target tumours were manually contoured. Values used in the simulated scanner were as follows: random fraction, 0.07; scatter fraction, 0.37; sensitivity, 7.4; and true counts/kBq/s and PSF, 4.9 mm. The images were projected for obtaining sinograms in which the desired Poisson noise level was introduced and reconstructed using OSEM (two iterations and 24 subsets) with CT-based attenuation correction and without PSF correction. Images were in a 256 × 256 matrix with a voxel size of 2.058 mm × 2.058 mm × 4.250 mm. The tumours were simulated with an S/B ratio ~ 3.5 and a background activity of 13.3 kBq/ml. Seven lesions with volumes between 2.3 ml and 14.7 ml were generated Fig. 2 at the top shows a representative slice of the lesions) in four different noise environments, with varying acquisition times of 30 s, 60 s, 180 s and 360 s, corresponding to total counts of 1.58 × 10⁷, 3.16 × 10⁷, 9.48 × 10⁷ and 1.90 × 10⁸, respectively. The values of the background level noise of the nonfiltered images are shown in Table 1. The various filters described below were applied after the OSEM reconstruction.

2.1.3. Simulated clinical series

The PETSTEP simulator [15] was used as in the previous case to build the synthetic clinical images. In this case, the GE DLS PET/CT scanner was modelled, and the values were as follows: random fraction, 0.08; scatter fraction, 0.43; sensitivity, 6.4; and true counts/kBq/s and PSF, 5.1 mm. Reconstruction, as with the original images, was performed using a 2D-OSEM with CT-based correction without PSF correction, obtaining reconstructed images of 128 × 128 matrix with a voxel size of 3.906 mm × 3.906 mm × 4.250 mm. Synthetic realistic lesions were implanted in images from six patients: three head and neck and three lung and mediastinum. The lesions were modelled based on clinical images and were manually contoured in CT images and assigned an uptake level. The simulation was then performed using these contours. As in previous cases, the considered filters were applied after the reconstruction. Volumes were obtained via manual contouring by an expert radiation oncologist and were compared with the masks used

Table 1

Filter effect. Noise level input (%) (second column) and noise level output (%) in the rest of the columns. Intensity bias in signal in the output image is indicated in parentheses. Values corresponding to the spherical objects are at the top, and those corresponding to the simulated irregular series are at the bottom.

Spherical objects		Noise level output % (intensity bias %)					
S/B	Noise level input (%)	g3f	g5f	g7f	bf	adf	3Dwf
~20:1	23.1	22.7 (-0.1)	17.9 (-2.2)	15.0 (-4.9)	16.2 (-2.4)	9.9 (-0.5)	13.2 (-0.3)
~10:1	19.7	19.2 (-0.2)	14.1 (-2.7)	10.6 (-5.9)	12.1 (-2.4)	5.7 (-0.5)	8.8 (-0.7)
~5:1	14.5	14.2 (-0.2)	9.9 (-2.9)	6.8 (-6.0)	8.3 (-2.4)	3.6 (-0.5)	6.0 (-0.8)
~5:1HR	19.5	13.8 (-1.6)	9.5 (-3.7)	5.9 (-7.3)	7.6 (-3.4)	13.9 (-0.2)	5.7 (-1.8)
Irregular objects		Noise level output % (intensity bias %)					
Time [s]	Noise level input (%)	g3f	g5f	g7f	bf	adf	3Dwf
30	24.9	11.9 (-14.4)	6.6 (-27.7)	3.8 (-40.2)	10.2 (-8.9)	13.1 (-4.0)	7.8 (-8.2)
60	19.4	9.9 (-10.4)	6.0 (-21.4)	4.0 (-32.0)	8.2 (-5.8)	11.2 (-1.8)	7.9 (-3.1)
180	13.7	6.1 (-4.9)	3.6 (-16.8)	2.5 (-26.3)	5.5 (-3.5)	6.0 (-0.7)	4.5 (-1.1)
360	9.7	5.3 (-7.5)	3.4 (-16.0)	2.5 (-25.2)	5.0 (-3.3)	4.2 (-0.7)	4.3 (-0.5)

in the generation of the lesions.

2.2. Filters

The comparison was made using the filters most frequently used in segmentation tasks, according to the AAPM report [4]. Thus, the proposed 3D wavelet-based filter (3Dwf) was compared with a set of Gaussian kernels, commonly used in daily practice. Bilateral and anisotropic diffusion filtering were also included in the comparison, both with excellent edge-preserving properties. Other approaches included in the AAPM report [4], incorporating anatomical information from other modalities, have proven their usefulness; however, they can create artefacts when the anatomical-functional correlation is not correct, and thus will not be considered in this study.

2.2.1. 3D wavelet-based filter: 3Dwf

The proposed algorithm is based on spatially adaptive wavelet shrinkage with context modelling based on the correlation of neighbouring pixels. It has been described in detail in Huerga et al. [12].

In this study we have implemented some improvements: The most relevant difference is that the calculation is performed directly in 3D. In the study by Huerga et al. [12], the 3D estimation was performed by averaging the various directions in each voxel, but the result is incomplete. To obtain a determination of local variance for each coefficient, including the information on the neighbouring voxels in the three projections, we have based the wavelet transformation on dual-tree complex wavelet transform (DTCWT) in 3D described by Selesnick [17]. The DTCWT possesses excellent characteristics of shift invariance, is directionally selective and is less redundant than the stationary wavelet transform (SWT). Transform coefficients of the real and imaginary part are obtained by the application of real filters in each orientation, so that the procedures of the general theory of the wavelet transform are applicable. After the application of the DTCWT, the local variance determination of noise-free coefficients is obtained through the autocorrelation function in 3D (3D-ACF) and in the wavelet domain.

Fig. 1 compares, in a representative way, the result to be expected with the modifications taken into account in this study with respect to the previous study. It represents current 3D direct processing versus the 3D estimation that was previously performed [12] in a head and neck case. The PET-AS used is an adaptive threshold segmentation (ATS) solution described below because it was considered (as will be shown) the best possible solution. When averaging in each direction, some voxels are erroneously included (red arrow) or excluded (blue arrow). The application of the DTCWT, with much more directionality and the context determination including all the neighbours of each voxel (not only the contents in a given plane), leads to an improvement over the estimate by averaging. Table 5 includes the global differences that can

be expected respect 3D estimation according to [12] and the improvement implemented in this work.

Other minor changes refer to avoid variance stabilization techniques (VST) that were used in [12]. The tests showed that the application of a previous VST step does not produce notable differences; thus, they were eliminated, reducing the computational cost and the complexity of the code. This topic will briefly be addressed in the Discussion section.

2.2.2. Gaussian filter: g3f, g5f and g7f

The most widely used post reconstruction filter is the Gaussian filter, of which the Gaussian filter with full width at half maximum (FWHM) of 5 mm is the filter most commonly included in publications. This filter is simple to implement and has a low computational cost; however, the SNR gain competes with the edge preservation, depending on the FWHM used [7]. A 3D Gaussian filtering was applied to each series with a 3 mm, 5 mm and 7 mm FWHM kernel, named g3f, g5f and g7f, respectively.

2.2.3. Bilateral filter: bf

A previously optimised bf [18] was applied with a 6 mm FWHM spatial kernel for a 2.058 mm × 2.058 mm pixel size and a FWHM of 7 mm for a 3.906 mm × 3.906 mm pixel size. In the radiometric domain, the FWHM kernel was adapted to local activity. The bf edge preservation features have already been observed by other authors [7,18]. The filter optimization was based on a fit of SNR values and bias intensity with the proposed wavelet-based filtering (3Dwf). The spatial kernel determines the number of neighboring voxels contributing significantly to the averaging process. The intensity-dependent part modulates the values included in this averaging. To preserve the edges of an object, the width of the intensity kernel must be smaller than local contrast. But not smaller than noisy range, because it could remain untouched. Thus, parameters selection is critical for the bf. The partial volume effect, the noise characteristics of the PET image (with intensity-dependent values) complicates this process.

2.2.4. Anisotropic diffusion filter: adf

The adf has been used as a previous step in PET image segmentation by several authors [8,9]. We applied the adf model proposed by Perona and Malik [19]. The adf is an iterative filter that generates blurred images based on an anisotropic diffusion process. The diffusion function acts as an edge-stopping function. Different solutions can be applied to fit parametric values of this function. This requires noise estimation. A value based on a percentile of the accumulated histogram of the absolute values of the gradient is used in [9,19]. Median absolute deviation, more robust to outliers, is also proposed as noise estimator in [20]. In addition, this estimate can be applied inside or outside the iterations.

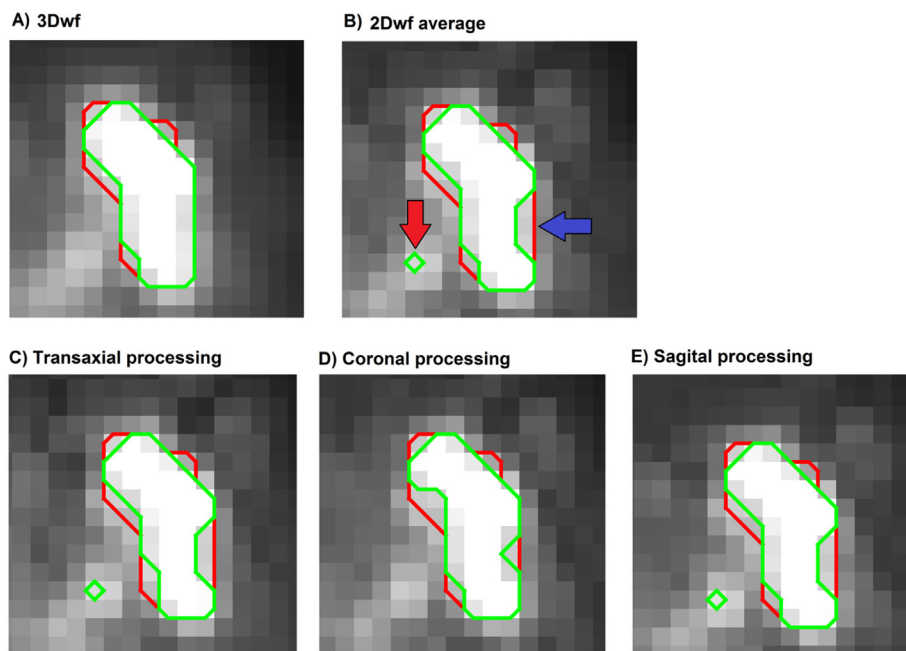


Fig. 1. Processing Comparison. Representative ATS head and neck lesion. In red, the simulated tumour (Ground Truth); in green, the result of ATS. Top: (A) 3Dwf; (B) 2Dwf average: the 3D estimate was made by averaging the 2D processing result of each projection. Bottom: (C), (D) and (E) are the result of processing each projection in 2D.

Test were performed comparing SNR values and intensity bias with the proposed wavelet-based filtering (*3Dwf*). In our case, the parametric values of this function have been estimated using the median absolute deviation of the image gradient as noise estimator in each iteration. The number of iterations has been limited to avoid oversmoothing, imposing 10 iterations for regular objects dataset and 15 for irregular objects dataset.

2.3. PET-AS procedures

Many segmentation procedures have been classified in the literature [5,6]. In this study, five have been selected according to the current vendor implementations [6]. These include the class of threshold-based algorithms (*thresholding*). Algorithms based on edge recognition are included (*gradient*) and those based on region of interest homogeneity (*region-based*). These algorithms, frequently used in clinical practice, are very sensitive to image noise, however. Finally, a method based on the statistical distribution of pixel intensity to partition the image has also been included (*clustering*).

2.3.1. Fixed threshold segmentation: FTS

The simplest segmentation scheme is based on the application of a fixed threshold by selecting the pixels above it. A threshold of 50% was used and applied to the maximum values average (to avoid spurious spikes 8 pixels were selected when it was possible) within a ROI, which involved the signal to be segmented.

The choice of threshold is arbitrary. In our case, a 50% threshold of the maximum was selected, following Hatt et al. [21], which indicates the robustness of this selection compared with a 42% threshold of the maximum (commonly used).

2.3.2. Adaptive threshold segmentation: ATS

Use of a single threshold value has limitations due to the large number of influencers. An ample bibliography [22,23] attempts to solve the problem of choosing a threshold adapted to various factors, such as acquisition conditions, equipment, S/B ratio and volume. In our case, the objective is not to evaluate the PET-AS algorithm, but to determine the influence denoising has on it; thus, the applied ATS is one that minimises the difference between the Ground Truth and the segmented volumes. This ATS only makes sense as a concept, without any practical

intent.

2.3.3. Watershed gradient segmentation: WGS

The watershed transform was applied to the gradient image in a similar manner as that used by Drever et al. [24]. The problem of oversegmentation associated with this technique was solved by morphological operations [25]. The choice of mark size (crucial question) was performed by a previous thresholding step using Otsu's method [26] to determine the number of N points above the threshold. We found from experimental tests that the adequate radius of the marks (disks) is $\sqrt{N/4}$ pixels for 256×256 matrix size and $\sqrt{N/2}$ pixels for 128×128 matrix size.

2.3.4. Adaptive region growing: ARG

An algorithm for seeded region-growing based on similarity of intensities proposed by Li et al. [27] was implemented. Via this algorithm, each pixel value is compared to the current cluster intensity average and is incorporated if it is within threshold T. To make it adaptive, the threshold T should vary from 0% to 100% in increments of 1%. The algorithm is stopped when a variation of volumes exceeds a certain magnitude. This algorithm is very sensitive to the initial seed value. This produces an “all-or-none” effect, in which all pixels (including the background) or none are selected. Constraints were applied based on a rough ROI, manually contoured to limit the tumour boundary and to choose the preliminary threshold.

2.3.5. Affinity propagation clustering: AP

We used the affinity propagation (AP) algorithm proposed by Foster et al. [28,29]. This method uses a similarity metric between the data points along the grey-level histogram of the image, then AP to cluster the intensities based on this metric.

The problem of labelling was solved using an optimum value for each filter used. It was considered as label optimum value the obtained for the sphere with diameter of 22 mm (intermediate size) in the medium contrast acquisitions for the IEC phantom. It was also necessary to use a rough manually contoured ROI to obtain the correct labelled cluster.

Table 2

Blur measure: The second column shows the average edge width of nonfiltered images (*nf*). The increase of the width with respect to *nf* is indicated for each filter. Spherical objects are located at the top and irregular series at the bottom.

Spherical objects		Increase of the width with respect to <i>nf</i> (in pixels)					
S/B	Width of <i>nf</i> image (in pixels)	<i>g3f</i>	<i>g5f</i>	<i>g7f</i>	<i>bf</i>	<i>adf</i>	<i>3Dwf</i>
~20:1	4.4	0.0	1.1	2.3	0.5	1.1	0.1
~10:1	4.6	0.0	0.5	1.5	1.3	1.3	0.4
~5:1	4.0	0.1	1.4	2.6	1.3	1.6	1.1
~5:1HR	4.6	0.6	1.5	3.6	1.0	1.6	0.9
	Mean	0.2	1.1	2.5	1.0	1.4	0.6
Irregular objects		Increase of the width with respect to <i>nf</i> (in pixels)					
Time [s]	Width of <i>nf</i> image (in pixels)	<i>g3f</i>	<i>g5f</i>	<i>g7f</i>	<i>bf</i>	<i>adf</i>	<i>3Dwf</i>
30	4.1	0.8	2.4	3.8	1.5	1.6	2.1
60	4.7	2.0	2.4	3.0	2.7	3.3	2.3
180	4.9	1.6	2.9	3.8	1.8	2.4	1.4
360	5.3	1.1	2.4	3.7	2.6	3.3	1.5
	Mean	1.4	2.5	3.6	2.1	2.6	1.8

2.4. Segmentation evaluation

The coincidence of shape on segmented volume with the Ground Truth was evaluated. The Dice metric (Dice similarity coefficient, DSC) and classification error (CE) were used. These are defined as [6]:

$$DSC = \frac{2|A \cap B|}{|A| + |B|} \quad (5)$$

$$CE = \frac{FP + FN}{|A|} \quad (6)$$

where A is the Ground Truth (reference volume), B is the measured volume to be evaluated (segmented volume), FP (false positive) is the volume included erroneously in segmentation (does not belong to the Ground Truth) and FN (false negative) is the volume not included in segmentation.

DSC provides a measure of overlap between the two volumes. It is normalised so that with a perfect coincidence, DSC = 1 is obtained. If only half of the evaluated volume coincides with the reference, then the DSC = 0.5. Several authors [30,31] consider that values of DSC > 0.7 represent a good result for a PET-AS. CE represents the segmentation error, both for excess or lack. Mean CE and associated standard deviation (SD) can be used to estimate the accuracy and precision of the segmentation algorithm associated with a denoising procedure.

A blurring measure was introduced using the method described by Marziliano et al. [32], which performed an objective blur estimation by computing the width average of all horizontal and vertical edges in the image. In short, the algorithm measures the edge width by iterating in each row (and column) and looking for the edge ends. The found width is accumulated in a total edge width counter and then divided between the number of borders found. The method requires an edge detector (usually Sobel), but it is very sensitive to image noise. In our case, the reference mask to locate and quantify only the edges of interest was used, thus preventing the possibility of finding spurious edges due to noise. This metric is a rough width edge estimate and its value should not be taken in isolation. This index was applied in the same manner to the various filters in the study and it will be used in the Discussion to establish a relationship between their values and the considered filters. It also has the advantage of being very simple to apply.

3. Results

3.1. Filters in phantom series

Table 1 summarises the filter effect for both phantom studies. The noise level (evaluated as standard deviation/average × 100) obtained

from various ROIs in the background region is indicated in both the input series and after filter application. We include in parentheses an estimate of the intensity bias. The intensity differences when applying various filters depends on the object size. We used a global score evaluated by means of ROI for each object and determined the mean value difference for each of them with respect to the nonfiltered image. The final index that is shown is the average response of all the objects. To avoid bias in the evaluation, the ROIs were identical for each data series.

As shown, the *g3f* filter barely reduces the noise level in spherical object series (*IEC-phantom*). This is due to pixel size of these series (3.906 mm), reconstructed in a 128 × 128 matrix. This does not occur in the case of irregular object series (*simulated phantom*), with a pixel size inferior to the FWHM of this filter. As the Gaussian kernel size increases, the noise level progressively decreases, as shown. Normally the filtering process involves a loss of signal intensity. As expected, Gaussian filters decrease the noise level at the expense of a strong loss of signal intensity, with this loss increasing with the kernel width used. The *bf*, *adf* and *3Dwf* are designed to minimise this intensity loss. These filters show a reduction in the noise level comparable to *g5f* or *g7f*, with a much lower signal intensity reduction (from table, the intensity bias and noise decreased ratio is greater than 1 for gaussian filters and below 1 for edge preserving filters). In particular, this table shows the good parameter adjustment implemented in *bf* and *adf*.

In order to better characterise the proposed filter, refer to Table 2, which shows the blurring measure of each dataset obtained by the Marziliano method [32]. To consider only the effect due to the filter, the results show the average edge width difference with respect to the nonfiltered images.

To measure the filter-induced blurring, the width of the nonfiltered images has been subtracted in each case due to the high variability in the average edge width of nonfiltered images. Tests (not shown here) with various stopping criteria for the OSEM algorithm show that the reason for these differences is probably due to the different convergence rates of the OSEM method.

The results in Table 2 are consistent with those in Table 1. In the case of the *g3f*, *g5f* and *g7f* filters, the blurring increase matches the loss of signal intensity. As shown, the blurring degree induced by the non-linear filters, *bf*, *adf* and *3Dwf*, can be quantified and is comparable to *g3f*. As shown in both tables, the proposed filter *3Dwf* shows a more appreciable compromise between noise reduction, maintaining signal intensity and preserving edge.

Fig. 2 shows, in a representative manner, the behaviour of the ARG and WGS algorithms implemented for the series, with irregular objects under various noise reduction procedures. As indicated in the caption,

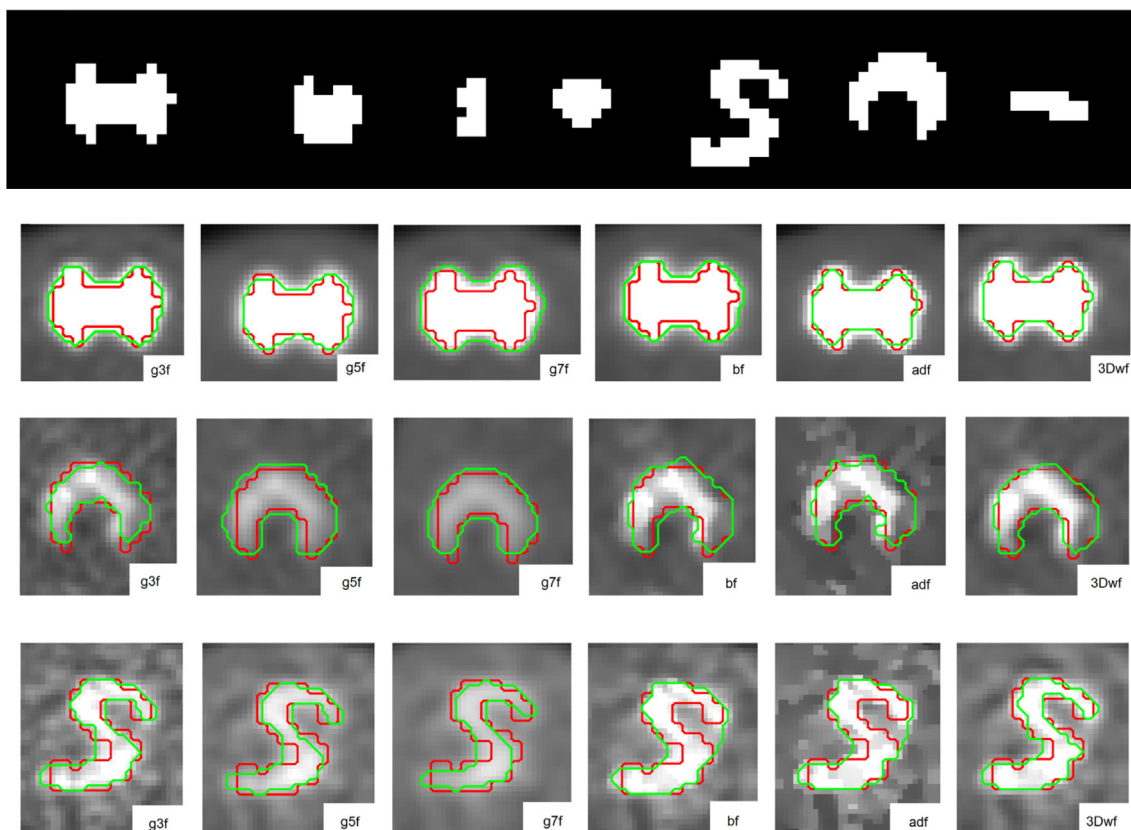


Fig. 2. Representative segmentation result of irregular object. First Row: Representative slice of the lesions (evaluation mask), outlined in red below. Second row: ARG segmentation “tie” object. (DSC, CE) measures in this slice are g3f (0.88, 0.26), g5f (0.89, 0.23), g7f (0.79, 0.54), bf (0.86, 0.33), adf (0.94,0.13), 3Dwf (0.94,0.13). Noise level before denoising = 9.7% (low noise). Third row: AP segmentation “croissant” object. (DSC, CE) measures in this slice are g3f (0.87, 0.23), g5f (0.84, 0.38), g7f (0.86, 0.31), bf (0.90, 0.22), adf (0.90, 0.19), 3Dwf (0.92, 0.18). Noise level before denoising = 19.4% (medium noise). Fourth row: WGS segmentation “S” object. (DSC, CE) measures in this slice are g3f (0.83, 0.33), g5f (0.78, 0.41), g7f (0.77, 0.42), bf (0.80, 0.45), adf (0.80, 0.46), 3Dwf (0.83, 0.33). Noise level before denoising = 24.9% (high noise).

three different noise levels have been considered. The values of the metrics used in each slice are also indicated. As presented, filtration using 3Dwf is shown to be more polyvalent, obtaining better performance in all cases. The positive result obtained by the filter g3f in the “S” object can be observed. The morphological operations implemented in WGS, prior to clustering, perform a process of filling objects in the foreground and noise reduction in the background. This means that low-filter methods such as g3f, which produce less smoothing and preserve edges better, benefit from this segmentation procedure.

Table 3 shows the mean values of the DSC and CE metrics against

each filter and the segmentation method on the phantom series with spherical inserts including only the reconstructions of 128 × 128 matrix size. Table 4 shows these mean values for the irregular inserts series.

As indicated in the Table 3 caption, the WGS and ARG algorithms are unable to segment smaller spheres (10- and 13-mm diameters) due to the resolution (128 × 128 with 3.906 mm/pixel) and implementation; thus, they were excluded from the evaluation (this exclusion was made for all filtering schemes).

It is worthwhile to address the effect of small objects on these two

Table 3

Mean and standard deviation (in parentheses) of DSC and CE metrics for spherical inserts (*with this resolution the WGS and ARG implementation are not able to segment the smaller spheres).

Filter	DSC					CE				
	FTS	ATS	WGS*	ARG*	AP	FTS	ATS	WGS*	ARG*	AP
g3f	0.81 (0.10)	0.88 (0.05)	0.84 (0.07)	0.70 (0.17)	0.83 (0.18)	0.33 (0.16)	0.24 (0.10)	0.32 (0.20)	0.57 (0.27)	0.27 (0.22)
g5f	0.85 (0.07)	0.88 (0.06)	0.83 (0.07)	0.71 (0.16)	0.84 (0.17)	0.30 (0.15)	0.25 (0.12)	0.36 (0.22)	0.69 (0.44)	0.25 (0.22)
g7f	0.82 (0.13)	0.87 (0.07)	0.73 (0.17)	0.69 (0.15)	0.80 (0.20)	0.48 (0.59)	0.25 (0.14)	0.42 (0.22)	0.77 (0.55)	0.30 (0.28)
bf	0.83 (0.09)	0.88 (0.05)	0.84 (0.07)	0.70 (0.16)	0.86 (0.17)	0.31 (0.15)	0.23 (0.14)	0.32 (0.19)	0.66 (0.39)	0.28 (0.30)
adf	0.83 (0.08)	0.88 (0.06)	0.79 (0.14)	0.69 (0.19)	0.84 (0.16)	0.31 (0.17)	0.24 (0.11)	0.37 (0.22)	0.60 (0.25)	0.32 (0.41)
3Dwf	0.86 (0.06)	0.88 (0.06)	0.85 (0.06)	0.74 (0.12)	0.87 (0.11)	0.28 (0.14)	0.24 (0.10)	0.31 (0.17)	0.55 (0.27)	0.26 (0.20)

Table 4
Mean and standard deviation (in parentheses) of DSC and CE metrics for irregular inserts (*IEC-phantom*).

Filter	DSC					CE				
	FTS	ATS	WGS	ARG	AP	FTS	ATS	WGS	ARG	AP
g3f	0.79 (0.07)	0.85 (0.05)	0.81 (0.06)	0.83 (0.05)	0.74 (0.14)	0.51 (0.23)	0.31 (0.10)	0.37 (0.15)	0.31 (0.11)	0.69 (0.69)
g5f	0.67 (0.11)	0.80 (0.07)	0.77 (0.06)	0.81 (0.06)	0.76 (0.08)	1.07 (0.49)	0.40 (0.13)	0.44 (0.15)	0.39 (0.13)	0.52 (0.12)
g7f	0.49 (0.17)	0.78 (0.07)	0.75 (0.06)	0.79 (0.06)	0.76 (0.07)	2.59 (1.64)	0.44 (0.14)	0.47 (0.14)	0.42 (0.12)	0.53 (0.12)
bf	0.80 (0.10)	0.87 (0.06)	0.82 (0.06)	0.85 (0.08)	0.84 (0.07)	0.41 (0.16)	0.27 (0.12)	0.35 (0.13)	0.30 (0.15)	0.37 (0.22)
adf	0.79 (0.11)	0.87 (0.08)	0.80 (0.09)	0.84 (0.08)	0.81 (0.12)	0.40 (0.17)	0.29 (0.17)	0.45 (0.35)	0.32 (0.16)	0.38 (0.19)
3Dwf	0.85 (0.05)	0.88 (0.05)	0.84 (0.05)	0.87 (0.07)	0.86 (0.05)	0.33 (0.12)	0.24 (0.11)	0.31 (0.09)	0.27 (0.13)	0.29 (0.11)

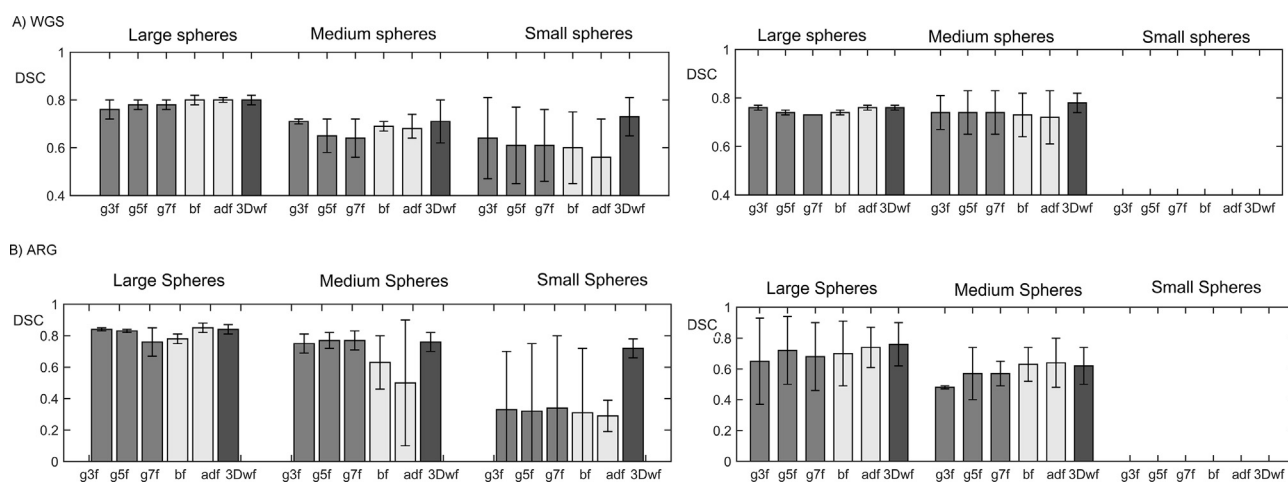


Fig. 3. Effect of the object size for the WGS (top) and ARG (bottom) algorithms on acquisition $\sim 5:1$ HR (left) and $\sim 5:1$ (right). The DSC values are grouped in three bins and the error bars represent the range within each bin.

schemes of segmentation. Fig. 3 compares the effect of the object size for the WGS and ARG algorithms on low contrast acquisition with matrix size of 256×256 and 128×128 by means of DSC values. To provide better visualisation of data, the results are grouped in three bins: large spheres (37–28 mm), medium-sized spheres (22–17 mm) and small spheres (13–10 mm); the error bars represent the range within each bin. Using the 128×128 matrix reconstruction (right) there are no large differences between the various segmentation schemes; however, the algorithms are unable to segment the small spheres. In the case of the 256×256 matrix reconstructions (left), the segmentation of these spheres is performed, showing an evident improvement using the *3Dwf* in both algorithms.

FTS filtering is very dependent on threshold choice. Thus, the result of the first column in Table 3 should be taken simply as a sample of the great influence of the filtering procedure in the segmentation processes. The ATS algorithm provides the optimal solution: in spherical objects, all the filters give the same result; in irregular objects, slight differences can be seen supporting the proposed procedure (*3Dwf*). In general, as shown in both tables, denoising procedures designed to preserve edges provide better results than those that do not. The *g3f* can be partially included in this statement with certain segmentation methods (as previously stated with WGS).

The spherical inserts dataset describes the filter segmentation variation at different S/B ratios. Fig. 4 shows DSC and CE mean values obtained, averaging all segmentation methods for each filter in high, medium and low contrasts. As can be observed, for all filters, diminishing the contrast results in a worsening of the segmentation process from high contrast to medium or low contrast, to assess this aspect it is

important to observe the strong increase in SD reflected in the error bars for all filters. The irregular objects dataset describes the segmentation differences at various input noise levels. Fig. 5 shows the DSC and CE mean values obtained, averaging all segmentation methods for each filter. Gaussian filters are affected significantly by noise level input. Of these, *g3f* exhibits the best behaviour in the distinct noise scenarios. The *bf* shows less dependence on noise, although in high-level noise conditions having DSC values below 0.8. The *adf* shows greater differences when varying the noise conditions. The proposed *3Dwf* is stable in noise conditions with DSC values higher than 0.8 and CE in a range of 0.35–0.23, much lower than the other filters. This stability is due to the noise estimation included in the filtering algorithm; thus, it is more adaptive to noise conditions.

The global error that can be expected with each segmentation method is shown in Table 5. Within Gaussian filters, smaller CE values are found with low filtering, in which edges remain with minor changes, despite the images having more noise (e.g. *g3f*). Nonlinear filters have a better performance with a lower error and SD. The *3Dwf* produces a noticeable improvement in segmentation task relative to the other denoising procedures. In case of irregular inserts, mean error below 30% with SD of 12% demonstrates how the segmentation methods considered are reinforced by this denoising procedure. Also, the global CE values obtained by 3D estimation according to previous work [12] have been included. As expected, *3Dwf* shows a slight improvement when considering irregular inserts due to the greater directionality of decomposition base used; this was shown in Fig. 1.

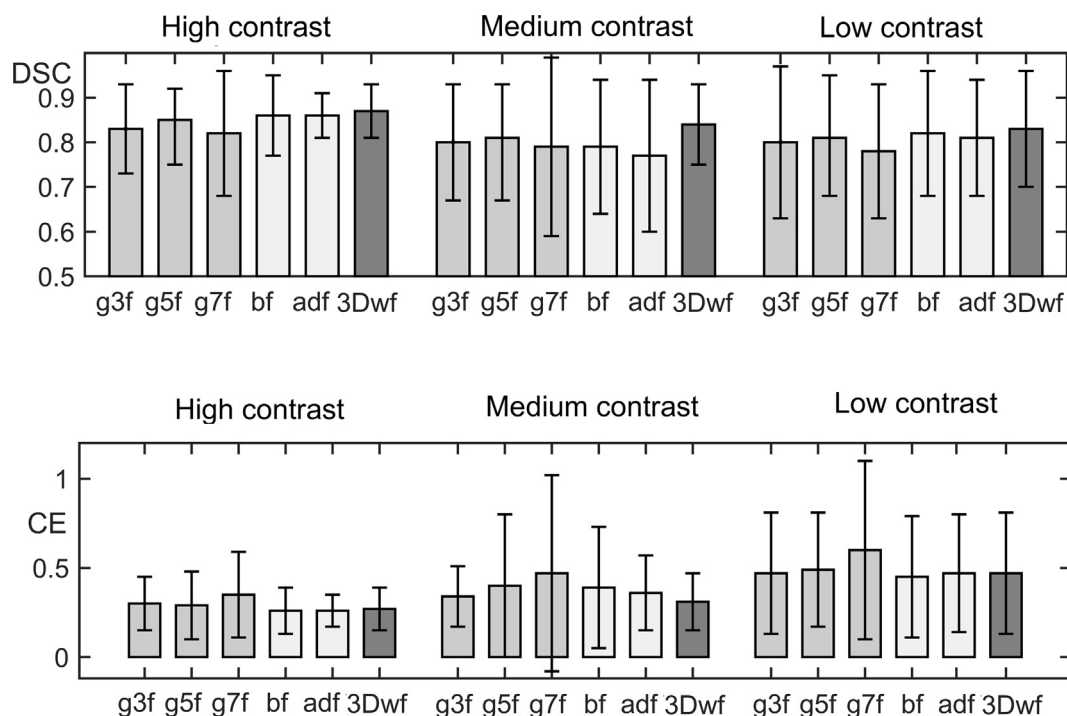


Fig. 4. Effect of contrast variation (S/B ratio). DSC and CE values averaging all segmentations on spherical inserts (IEC-phantom). Error bars represent one standard deviation from the mean.

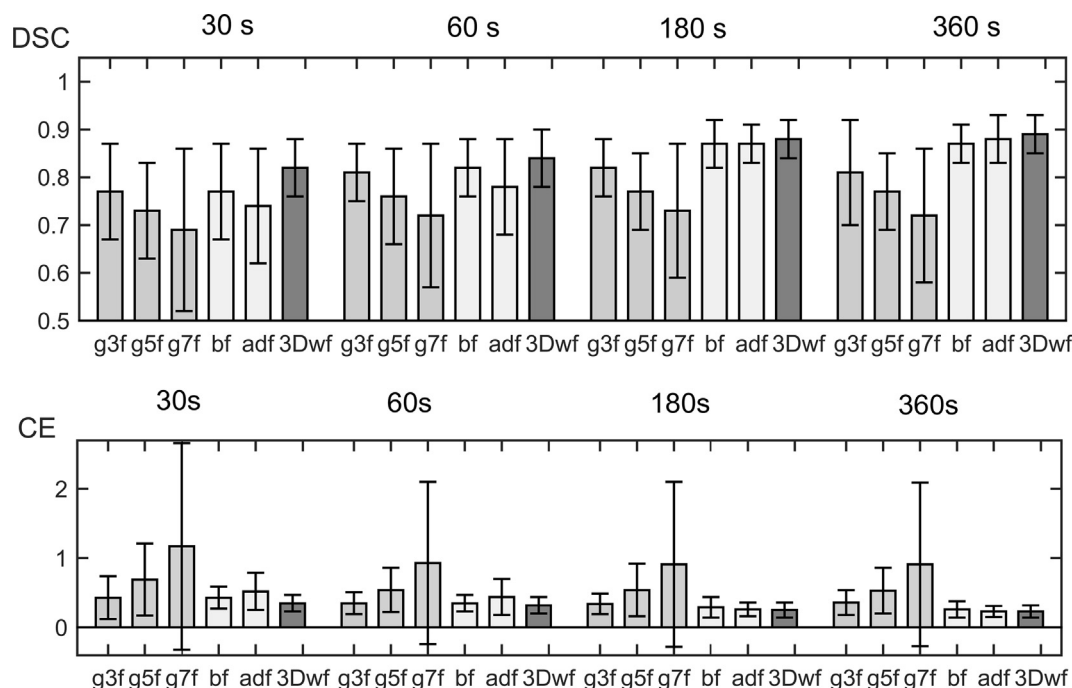


Fig. 5. Effect of noise level on input. DSC and CE values averaging all segmentations on irregular objects (simulated phantom). Error bars represent one standard deviation from the mean.

3.2. Filters in clinical series

Fig. 6 shows the result of manual contouring performed by the radiation oncologist involving various filters in a mediastinum lesion; and Table 6 shows the DSC and CE mean values for the six clinical cases considered: three head and neck and three lung and mediastinum. It is not possible to establish a statistical correlation due to the evaluation of only a few cases; however, the experience of this test indicates that use of filters with edge preservation properties leads to an improvement in

manual segmentation. A possible explanation is obtained from Fig. 6: the excessive presence of noise in g3f and the over-smoothing in g7f produces a worsening in manual contouring. In this example adf shows poor performance, however in global good results are obtained with it.

4. Discussion

We have presented segmentation properties of a nonlinear wavelet-based filter (3Dwf). This version is improved when compared with

Table 5

Mean classification error, associated standard deviation and rank associated with each filter, averaging all the segmentations. Regular and irregular object contribution is also indicated.

Filter	g3f	g5f	g7f	bf	adf	3Dwf
Mean CE	0.39	0.46	0.66	0.34	0.37	0.31
Standard dev	0.30	0.34	0.88	0.23	0.25	0.17
Range [max, min]	[3.15, 0.05]	[2.08, 0.02]	[4.93, 0.03]	[1.71, 0.02]	[1.80, 0.02]	[0.94, 0.05]
Mean CE	0.34	0.36	0.44	0.35	0.36	0.32
Standard dev	0.22	0.29	0.44	0.28	0.28	0.21
Range [max, min]	[0.95, 0.05]	[2.00, 0.02]	[2.57, 0.03]	[1.71, 0.02]	[1.80, 0.02]	[0.94, 0.05]
Mean CE	0.44	0.56	0.89	0.34	0.37	0.29
Standard dev	0.36	0.35	1.12	0.16	0.22	0.12
Range [max, min]	[0.35, 0.18]	[2.08, 0.22]	[4.93, 0.25]	[0.92, 0.14]	[1.38, 0.13]	[0.60, 0.13]

previous studies [12], by applying 3D context implicitly: from the 3D-ACF and using the DTCWT described by Selesnick [17] as representation in the 3D-wavelet domain.

Another minor change refers to not including the VST step. In this study, we have not found notable differences with and without VST; and it is remained as an optional issue. In addition, the use of VST is not without controversy. Using VST is subject to parameters that if they are poorly determinate leading to inaccurate results with losing clinical information. We propose as future work the adequate determination of the parameters of VST in PET, and the need to include this step in denoising schemes under the wavelet transform.

To show the proposed filter properties, a comparison was performed with various widely used filtering methods and in various segmentation frameworks. All the filters were characterised, showing the input and output SNR and bias in the intensity produced Table 1. A blurring metric based on the measurement of the average image edge width was introduced, using a simple method [32] Table 2. This metric can be useful for adjusting parameters in nonlinear filters and can serve as a reference when comparing results between studies.

Within the filters used for comparison purposes, *bf* and *adf* have been included. These filters, such as that we proposed, share border preservation features. However, they strongly depend on parameter adjustment by the user [17] because the same adjustment might not be valid from one case to another. The solution that we present is unique, without dependent parameters. It is based on the autocorrelation function determination, obtained from the power spectral density, which describes how the signal energy is distributed in the frequency domain. It is easily obtained in the PET scanner for the reconstruction used, given that its acquisition forms part of the periodic controls to which they are subject.

The proposed noise reduction method improves the results of

segmentation in all considered cases. It is necessary to point out that although the differences are not yet statistically significant in the scenarios described, a clear positive influence is shown from the *3Dwf* when compared with other evaluated filters in the considered segmentation procedures. From the results on phantoms, by averaging all the objects and series (both irregular and regular), the DSC value for *3Dwf* is 0.85 (0.98–0.50) and in order from the highest to the lowest value, 0.83 (0.99–0.44), 0.82 (0.99–0.19), 0.81 (1.0–0.39), 0.79 (0.99–0.43) and 0.76 (0.99–0.00) for the *bf*, *adf*, *g3f*, *g5f* and *g7f*, respectively.

3Dwf was also shown to be more stable under conditions of low contrast and high noise, showing lower spread of segmentation results. In contrast assessment, the proposed filter has a mean CE and SE of 0.29 ± 0.12 , compared with the values 0.34 ± 0.16 and 0.37 ± 0.22 of the *bf* and *adf* respectively (leading to a decrease in error rate of approximately 15%); and 0.44 ± 0.36 , 0.56 ± 0.035 for Gaussian filters *g3f* and *g5f* respectively (decreasing the error rate more than 35%).

Recently, McGurk et al. [11] performed an interesting evaluation of the influence of filtering on segmentation. They obtained a fit DSC model for a series of explanatory variables (scan duration, contrast, filter, and segmentation method). As far as we know, no other studies make a similar assessment. However, some of the results from McGurk's study do not match ours. In particular, the filter with the best tradeoff relationship between image smoothing and edge preservation is *g5f*. In this reference *bf* shows poor results, being necessary a Gaussian pre-filtering to achieve better results. However, we found that better results are obtained by filters designed to preserve edges such as *bf*, *adf* and *3Dwf*. One of the differences with the study by McGurk et al. [11] is the parameter adjustment for the *bf*. They were performed fitted to the *g5f*; and in our case fitted to the *3Dwf*, thus, results might not be comparable.

We have presented an interesting exercise to evaluate the difficulties of the radiation oncologist when facing contouring of volumes in clinical series. With the few cases evaluated, it was not possible to establish a statistical correlation. The object of this study was not to cover a large number of situations and the complexity of the clinical environment. However, the test performed appears to indicate that the postreconstruction filter significantly affects the appearance of the final image. The presence of a noisy environment and more undefined edges can cause operator "discomfort," which could affect the final result of the contouring. With these six cases, 36 volumes have been generated in two pathologies. From this experiment, the best results, i.e. the contoured volume, which was closer to the simulated volume, were achieved by using the filters having good edge preservation properties: the *bf* and *3Dwf*. A more in-depth investigation, based on the operator's perception, will be the subject of a future study.

Finally, with regard to denoising role in segmentation, advanced methods of segmentation could make previous steps of noise reduction unnecessary (even using non-filtered images): Hatt et al. [21] it shows a segmentation method (FLAB) that take into account the noise properties in its statistical modeling. In our study, it has been observed when considering the good properties of *g3f* combined with WGS. Specifically, the benefit obtained is through the morphological operations to

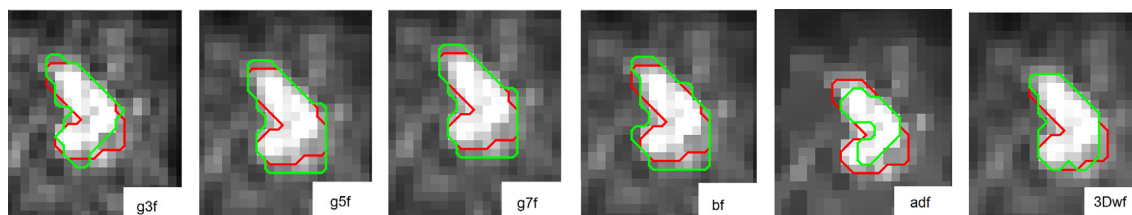


Fig. 6. Representative manual segmentation result of mediastinal lesion. In red, the simulated tumour, in green, the result of manual contouring. (DSC, CE) measures in this slice are *g3f* (0.86, 0.28), *g5f* (0.86, 0.31), *g7f* (0.87, 0.30), *bf* (0.84, 0.38), *adf* (0.67, 0.47) and *3Dwf* (0.90, 0.20).

Table 6

Mean values in DSC and CE and maximum and minimum range for six patients manually contoured under different filters.

Manual Contouring	g3f	g5f	g7f	bf	adf	3Dwf
DSC	0.87	0.88	0.86	0.90	0.90	0.90
[max, min]	[0.92–0.75]	[0.96–0.79]	[0.92–0.77]	[0.97–0.77]	[0.97–0.70]	[0.97–0.79]
CE	0.25	0.26	0.31	0.20	0.22	0.20
[max, min]	[0.55–0.10]	[0.48–0.10]	[0.55–0.10]	[0.56–0.06]	[0.44–0.07]	[0.49–0.07]

avoid over-segmentation. Perhaps this is the reason for the lack of discussion in the compilations [5,6], which we have discussed in the introduction. However, we thought that many others PET-AS would show an improvement, with better noise processing. In this study we have included the most commonly segmentation schemes in clinical practice, and some results can be derived from our work and although some of them might seem obvious, they are important and they are not often considered in clinical practice.

5. Conclusion

We have proposed an improvement of a nonlinear wavelet-based filter that evaluates the 3D context for enhancing the filtering effect and edge preservation. The proposed filter has been characterised in detail and the effect on segmentation tasks has been presented. The inclusion of this type of filter in segmentation procedures represents a promising tool for reinforcing its accuracy and precision.

6. Funding

This study was supported by Foundation for Biomedical Research of La Paz University Hospital (Spain) Dr. Luis Álvarez 2016.

References

- González-López A, Morales-Sánchez J, Larrey-Ruiz J, Bastida-Jumilla MC, Verdú-Monedero R. Portal imaging: performance improvement in noise reduction by means of wavelet processing. *Phys Med* 2016;32:226–31. <https://doi.org/10.1016/j.ejmp.2015.09.016>.
- Gui L, Li C, Yang X. Medical image segmentation based on level set and isoperimetric constraint. *Phys Med* 2017;42:162–73. <https://doi.org/10.1016/j.ejmp.2017.09.123>.
- Boellaard R. Standards for PET image acquisition and quantitative data analysis. *J Nucl Med* 2009;50(suppl 1):11S–20S. <https://doi.org/10.2967/jnumed.108.057182>.
- Rousset OG, Ma Y, Evans AC. Correction for partial volume effects in PET: principle and validation. *J Nucl Med* 1998;39:904–11.
- Foster B, Bagci U, Mansoor A, Xu Z, Mollura DJ. A review on segmentation of positron emission tomography images. *Comput Biol Med* 2014;50:76–96. <https://doi.org/10.1016/j.compbiomed.2014.04.014>.
- Hatt M, Lee JA, Schmidlein CR, El Naqa I, Caldwell C, De Bernardi E, et al. Classification and evaluation strategies of auto-segmentation approaches for PET: report of AAPM task group No. 211. *Med Phys* 2017;44:e1–42. <https://doi.org/10.1002/mp.12124>.
- Geets X, Lee JA, Bol A, Lonnet M, Grégoire V. A gradient-based method for segmenting FDG-PET images: methodology and validation. *Eur J Nucl Med Mol Imaging* 2007;34:1427–38. <https://doi.org/10.1007/s00259-006-0363-4>.
- Belhassen S, Zaidi H. A novel fuzzy C-means algorithm for unsupervised heterogeneous tumor quantification in PET. *Med Phys* 2010;37:1309–24. <https://doi.org/10.1118/1.3301610>.
- Abdoli M, Dierckx RAJO, Zaidi H. Contourlet-based active contour model for PET image segmentation. *Med Phys* 2013;40:82507. <https://doi.org/10.1118/1.4816296>.
- Hanzouli H, Lapuyade-Lahorgue J, Monfrini E, Delso G, Pieczynski W, Visvikis D, et al. PET/CT image denoising and segmentation based on a multi observation and a multi scale Markov tree model. *IEEE Nucl Sci Symp Conf Rec* 2013. <https://doi.org/10.1109/NSSMIC.2013.6829281>.
- McGurk RJ, Smith VA, Bowsher J, Lee JA, Das SK. Influence of filter choice on 18F-FDG PET segmentation accuracy determined using generalized estimating equations. *Phys Med Biol* 2013;58:3517–34. <https://doi.org/10.1088/0031-9155/58/11/3517>.
- Huerga C, Castro P, Corredoira E, Coronado M, Delgado V, Guibelalde E. Denoising of PET images by context modelling using local neighbourhood correlation. *Phys Med Biol* 2017;62:633–51. <https://doi.org/10.1088/1361-6560/62/2/633>.
- Boellaard R, Delgado-Bolton R, Oyen WJG, Giammarile F, Tatsch K, Eschner W, et al. FDG PET/CT: EANM procedure guidelines for tumour imaging: version 2.0. *Eur J Nucl Med Mol Imaging* 2014;42:328–54. <https://doi.org/10.1007/s00259-014-2961-x>.
- Berthon B, Marshall C, Edwards A, Evans M, Spezi E. Influence of cold walls on PET image quantification and volume segmentation: a phantom study. *Med Phys* 2013;40:82505. <https://doi.org/10.1118/1.4813302>.
- Berthon B, Haggström I, Apte A, Beattie BJ, Kirov AS, Humm JL, et al. PETSTEP: generation of synthetic PET lesions for fast evaluation of segmentation methods. *Phys Med* 2015;31:969–80. <https://doi.org/10.1016/j.ejmp.2015.07.139>.
- Deasy JO, Blanco AI, Clark VH. CERR: a computational environment for radiotherapy research. *Med Phys* 2003;30:979–85. <https://doi.org/10.1118/1.1568978>.
- Selesnick IW, Baraniuk RG, Kingsbury NG. The dual-tree complex wavelet transform. *IEEE Signal Process Mag* 2005;22:123–51. <https://doi.org/10.1109/MSP.2005.1550194>.
- Hofheinz F, Langner J, Beuthien-Baumann B, Oehme L, Steinbach J, Kotzerke J, et al. Suitability of bilateral filtering for edge-preserving noise reduction in PET. *EJNMMI Res* 2011;1:23. <https://doi.org/10.1186/2191-219X-1-23>.
- Perona P, Malik J. Scale-space and edge detection using anisotropic diffusion. *IEEE Trans Pattern Anal Mach Intell* 1990;12:629–39. <https://doi.org/10.1109/34.56205>.
- Tsiotsios C, Petrou M. On the choice of the parameters for anisotropic diffusion in image processing. *Pattern Recogn* 2013;46:1369–81. <https://doi.org/10.1016/j.patcog.2012.11.012>.
- Hatt M, Cheze Le Rest C, Albarghach N, Pradier O, Visvikis D. PET functional volume delineation: a robustness and repeatability study. *Eur J Nucl Med Mol Imaging* 2011;38:663–72. <https://doi.org/10.1007/s00259-010-1688-6>.
- Erdi YE, Mawlawi O, Larson SM, Imbricco M, Yeung H, Finn R, et al. Segmentation of lung lesion volume by adaptive positron emission tomography image thresholding. *Cancer* 1997;80:2505–9. doi:10.1002/(SICI)1097-0142(19971215)80:12+ < 2505::AID-CNCR24 > 3.0.CO;2-F [pii].
- Biehl KJ, Kong F-M, Dehdashti F, Jin J-Y, Mutic S, El Naqa I, et al. 18F-FDG PET definition of gross tumor volume for radiotherapy of non-small cell lung cancer: is a single standardized uptake value threshold approach appropriate? *J Nucl Med* 2006;47:1808–12. <https://doi.org/10.1118/1.1808> [pii].
- Drever LA, Roa W, McEwan A, Robinson D. Comparison of three image segmentation techniques for target volume delineation in positron emission tomography. *J Appl Clin Med Phys* 2007;8:93–109.
- Gonzalez RC, Woods RE. *Digital Image Processing*, 3rd ed., 2007.
- Otsu N. A threshold selection method from gray-level histograms. *IEEE Trans Syst Man Cybern* 1979;9:62–6. <https://doi.org/10.1109/TSMC.1979.4310076>.
- Li H, Thorstad WL, Biehl KJ, Laforest R, Su Y, Shoghi KI, et al. A novel PET tumor delineation method based on adaptive region-growing and dual-front active contours. *Med Phys* 2008;35:3711–21. <https://doi.org/10.1118/1.2956713>.
- Foster B, Bagci U, Xu Z, Dey B, Luna B, Bishai W, et al. Segmentation of PET images for computer-aided functional quantification of tuberculosis in small animal models. *IEEE Trans Biomed Eng* 2014;61:711–24. <https://doi.org/10.1109/TBME.2013.2288258>.
- Foster B, Bagci U, Luna B, Dey B, Bishai W, Jain S, et al. Robust segmentation and accurate target definition for positron emission tomography images using affinity propagation. 2013 IEEE 10TH Int. Symp. Biomed. IMAGING, 2013, p. 1461–4.
- Zijdenbos AP, Dawant BM, Margolin RA, Palmer AC. Morphometric analysis of white matter lesions in MR images: method and validation. *IEEE Trans Med Imaging* 1994;13:716–24. <https://doi.org/10.1109/42.363096>.
- Zou KH, Warfield SK, Bharatha A, Tempany CMC, Kaus MR, Haker SJ, et al. Statistical validation of image segmentation quality based on a spatial overlap index. *Acad Radiol* 2004;11:178–89. [https://doi.org/10.1016/S1076-6332\(03\)00671-8](https://doi.org/10.1016/S1076-6332(03)00671-8).
- Marziliano P, Dufaux F, Winkler S, Ebrahimi T. A no-reference perceptual blur metric. *Proc Int Conf Image Process* 2002;1. <https://doi.org/10.1109/ICIP.2002.1038902>. III-57-III-60.